

Structure and regulation of the microtubule plus-end tracking protein Kar9

Anil Kumar^{1,4,6}, Sandro M. Meier^{1,2,6}, Ana-Maria Farcas^{2,6}, Cristina Manatschal^{1,5}, Yves Barral^{2*}, Michel O. Steinmetz^{1,3,7*}

¹Laboratory of Biomolecular Research, Division of Biology and Chemistry, Paul Scherrer Institut, CH-5232 Villigen PSI

²Institute of Biochemistry, ETH Zürich, CH-8093 Zürich, Switzerland

³University of Basel, Biozentrum, CH-4056 Basel, Switzerland

⁴Present address: ImmunOs Therapeutics AG, CH-8952 Schlieren, Switzerland

⁵Present address: Institute of Biochemistry, University of Zürich, CH-8057 Zürich, Switzerland

⁶Equal contribution

⁷Lead contact: michel.steinmetz@psi.ch

*Correspondence: yves.barral@bc.biol.ethz.ch and michel.steinmetz@psi.ch

This document is the accepted manuscript version of the following article:
Kumar, A., Meier, S. M., Farcas, A. M., Manatschal, C., Barral, Y., & Steinmetz, M. O. (2021). Structure and regulation of the microtubule plus-end tracking protein Kar9. *Structure*, 29(11), 1266-1278.e4. <https://doi.org/10.1016/j.str.2021.06.012>

This manuscript version is made available under the CC-BY-NC-ND 4.0 license
<http://creativecommons.org/licenses/by-nc-nd/4.0/>

SUMMARY

In many eukaryotes, coordination of chromosome segregation with cell cleavage relies on the patterned interaction of specific microtubules with actin filaments through dedicated microtubule plus-end tracking proteins (+TIPs). However, how these +TIPs are spatially controlled is unclear. The yeast +TIP Kar9 drives one of the spindle aster microtubules along actin cables to align the mitotic spindle with the axis of cell division. Here, we report the crystal structure of Kar9's folded domain, revealing spectrin repeats reminiscent of the +TIPs MACF/ACF7/Shot and PRC1/Ase1. Point mutations abrogating spectrin repeat-mediated dimerization of Kar9 reduced and randomized Kar9 distribution to microtubule tips, and impaired spindle positioning. Six Cdk1 sites surround the Kar9 dimerization interface. Their phosphomimetic substitution inhibited Kar9 dimerization, displaced Kar9 from microtubules, and affected its interaction with the myosin motor Myo2. Our results provide molecular-level understanding on how diverse cell types may regulate and pattern microtubule-actin interactions to orchestrate their divisions.

KEY WORDS

Microtubule plus-end tracking proteins; microtubule-actin crosstalk; structure-function relationship; protein regulation by phosphorylation

INTRODUCTION

In many eukaryotes, the spatial patterning of microtubule-actin interactions controls the appropriate positioning of the mitotic spindle and the cleavage apparatus relative to each other during cell division. This ensures that spindle elongation and cytokinesis segregate the sister chromatids equally between the two daughter cells (reviewed in (Barr and Gruneberg, 2007; D'Avino et al., 2015)). Thereby, these interactions contribute to genomic stability through generations. Furthermore, microtubule-actin interactions also determine the axis of cell division, which is of prime importance during asymmetric cell division or for tissue development (reviewed in (Kusch et al., 2003)). The spatial patterning of the interactions that microtubules and actin filaments entertain with each other also orchestrate a broad range of other cellular activities, including the motility of migratory cells (Wu et al., 2008) or the growth of axons (Alves-Silva et al., 2012). Therefore, understanding how cells spatially organize the crosstalk between the microtubule and actin cytoskeletons is paramount to deciphering how they control their architecture, coordinate spatial events and orient themselves in their environment.

In all systems studied so far, microtubule plus end-tracking proteins (+TIPs) play a major role in spatially orchestrating how cytoskeletal filaments interact with each other (reviewed in (Akhmanova and Steinmetz, 2008, 2015)). Some +TIPs modulate the dynamic behavior of microtubule tips throughout the cell. They include the End Binding proteins (EBs), the cytoplasmic linker proteins (CLIPs), the microtubule polymerase chTOG/XMAP215 and motor proteins, all of which contain microtubule-binding domains (reviewed in (Akhmanova and Steinmetz, 2008, 2015)). Other +TIPs in turn show more discrete cellular distributions as they primarily localize to the plus ends of a specific set of microtubules, generally at defined subcellular locations. These +TIPs nearly always contain binding sites for EBs, and are key specificity factors for the spatial patterning of microtubule interactions with other cellular components like, for example, actin filaments (reviewed in (Akhmanova and Steinmetz, 2008, 2015)). As such, they generally act in specific aspects of microtubule function, including the growth and guidance of axons, cell motility, and spindle positioning. These +TIPs, which we refer here to as “patterning +TIPs”, include the microtubule-actin crosslinking factors (MACF/ACF7/Shot, involved in axon growth and epithelial polarity; reviewed in (Sonnenberg and Liem, 2007)), SLAIN1/2 (implicated in axon development (van der Vaart et al., 2012)), the adenomatous polyposis coli protein (APC, involved in cell division and cancer; reviewed in (Nelson and Näthke, 2013)), PRC1/Ase1 (orchestrating the elongation of the mitotic spindle in most eukaryotes; reviewed in (Jiang et al., 1998; Pellman et al., 1995)) and Kar9 (karyogamy mutant 9 (Miller and Rose, 1998)).

The prototypical patterning +TIP Kar9 orchestrates the interactions between actin filaments and astral microtubules to drive the migration of the metaphase spindle towards the mother-bud neck (the pre-determined division plane) of budding yeast cells and facilitate the alignment of the spindle with the mother-bud axis (the division axis of the cell; reviewed in (Kusch et al., 2003; McNally, 2013)). Thereby, it ensures that spindle elongation pulls one set of sister-chromatids into the bud upon anaphase onset, while the reciprocal set is kept in the mother cell.

At the molecular level, Kar9 interacts with astral microtubules via its binding-partner Bim1, the orthologue of EB1, and with actin filaments through the actin-directed, type V myosin motor protein Myo2 (Hwang et al., 2003; Korinek et al., 2000; Miller and Rose, 1998; Yin et al., 2000). Strikingly, the function of Kar9 depends on its remarkably patterned localization: during metaphase, it localizes exclusively to the tip of a single or few astral microtubule(s) emanating from the older of the two spindle pole bodies (Hotz et al., 2012; Kusch et al., 2003; Kusch et al., 2002; Lengefeld et al., 2017; Liakopoulos et al., 2003; Maekawa et al., 2003) (SPBs, equivalent of centrosomes in animal cells). Myo2 then pulls this microtubule tip along actin cables towards the bud (Hwang et al., 2003; Liakopoulos et al., 2003). This makes the old SPB move and orient itself towards the bud, whereas the new one remains in the mother cell (Hotz et al., 2012; Pereira et al., 2000). Thus, the focused localization of Kar9 to only one microtubule aster assigns the old SPB to the bud and the new one to the mother cell, and concomitantly aligns the mitotic spindle with the axis of cell division, near the future cleavage plane. Therefore, the Kar9-mediated +TIP network is an excellent model system for studying at the molecular level how eukaryotic cells spatially pattern the interaction of specific microtubules with target cellular elements such as actin filaments.

Structurally, Kar9 consists of a folded, predominantly helical N-terminal domain (Kar9N) and an unstructured C-terminal region enriched in basic, serine and proline residues (Manatschal et al., 2016). Furthermore, Kar9N, which contains the critical S197 Cdk1 phosphorylation site (Liakopoulos et al., 2003; Maekawa and Schiebel, 2004; Moore and Miller, 2007), mediates the transient dimerization of full length Kar9 in vitro (Manatschal et al., 2016). Here, using an integrated structural biology, biophysical, biochemical and cell biology approach we characterized in detail the structural determinants of Kar9's dimerization and their functional relevance.

RESULTS

Crystal structure of the N-terminal domain of NcKar9

To assess the mechanism of Kar9 dimerization, we sought to solve the structure of its N-terminal domain (Kar9N) by X-ray crystallography. To generate well diffracting crystals, Kar9 orthologues from *Saccharomyces cerevisiae*, *Naumovozyma castellii*, *Saccharomyces kudriavzevii*, *Vanderwaltozyma polyspora*, *Kazachstania africana* and *Eremothecium cymbalariae* (Figure S1A) were cloned, recombinantly expressed and purified to homogeneity. The best crystals were obtained for *N. castellii* Kar9N (NcKar9N), which diffracted to a resolution of 3.3 Å (Table 1). The structure of NcKar9N was solved using the single anomalous dispersion method using a selenomethionine-labeled protein sample. The asymmetric unit of the crystal contained two molecules of NcKar9N, which are related by two-fold pseudosymmetry. With the exception of some presumably flexible loops, the electron density allowed to trace unambiguously the backbone of both NcKar9N molecules and to build most of the amino acid residue side chains (Figure S2). The structure of both NcKar9N molecules are very similar with a root-mean-square deviation of 0.7 Å over 290 C α backbone atoms.

The overall elongated, predominantly helical structure of NcKar9N is organized in three tandemly arranged subdomains, each connected by a short helical segment (Figure 1A). As illustrated in Figure 1B, these three subdomains show characteristics of spectrin repeats (SR), which form antiparallel, three-stranded α -helical coiled-coil structures (reviewed in (Djinovic-Carugo et al., 2002)); the SR coiled-coil helices are denoted A, B and C. The N-terminal SR1 is flanked by an N-terminal helix (H1) that packs against the SR1 helices A and B. Furthermore, a short helix (H5), which is inserted in the loop connecting helices A and B of SR2 packs against helices A and B of SR3. Mapping of the conserved residues (Figure S1A) on the surface of NcKar9N revealed that the sequence of SR1 of Kar9N is generally poorly conserved. However, several conserved residue patches were revealed on the surface of SR2 and SR3 (Figure 1C), which are likely to be relevant for Kar9 function.

Structural basis of NcKar9N dimerization

To test whether the self-association property observed for ScKar9N in vitro (Manatschal et al., 2016) is conserved in NcKar9N, we performed size exclusion chromatography followed by multi-angle light scattering (SEC-MALS) experiments (Figure 2C). Analysis of NcKar9N at 50 μ M (concentration injected onto the SEC column) and in the presence of 250 mM sodium chloride yielded an elution volume and molecular mass of 12.5 ml and 80.3 ± 0.3 kDa, respectively. This result suggests that NcKar9N, like ScKar9N, displays a tendency to dimerize

in solution at micromolar protein concentrations (calculated mass of the His-tagged NcKar9N monomer: 50 kDa).

To gather insights into the structural basis of Kar9N dimerization, we analyzed the packing of the NcKar9N molecules in the crystal. We found three crystallographic dimers with total buried surface area per molecule of 1549, 1177, and 851Å², respectively. We suspected that the dimer with the largest buried surface area to be functionally relevant. It is formed by antiparallel, symmetric contacts between the A and C and A' and C' helices of SR2 and SR2', and the A' and B' and A and B helices of SR3' and SR3, respectively (the prime discriminates the second molecule in the crystallographic dimer; Figure 2A). The two symmetric contact points in the crystallographic NcKar9N dimer are established by two sets of NcKar9 residues, namely F181, Q184, E185, F188, F288, E292, E299, and K303, and Y318', E322', K329', R343', F344', Q347', K350', and K351'. The side chains of these two sets of residues establish a network of hydrophobic and polar interactions across the dimer interface (Figure 2B). Notably, all these residues are well conserved in Kar9 orthologues (Figure S1A).

We probed the relevance of this crystallographic dimer by mutating the prominent and conserved interface residues F288 and F344 to alanines (NcKar9N-F288A/F344A). The far-ultra violet CD spectra and thermal unfolding profile recorded at 222 nm suggested that NcKar9N-F288A/F344A is properly folded, like the wild type protein (Figure S3). Next, we assessed the oligomerization state of NcKar9N-F288A/F344A by SEC-MALS. Analysis of NcKar9N-F288A/F344A under the same conditions as the wild type protein yielded an elution volume of 13.7 ml and a molecular mass of 49.0 ± 0.2 kDa (Figure 2C), consistent with a monomeric state. Thus, transient dimerization is a conserved property of Kar9 proteins, for which the two residues F288 and F344 of NcKar9, which are conserved among Kar9 orthologues (Figure S1A), are critical. Interestingly, the homo- and heterotypic dimerization of cytoskeletal proteins through spectrin-repeat-mediated interactions is a common property of spectrin-repeat-containing cytoskeletal proteins like, for example, α -actinin and spectrin (reviewed in (Liem, 2016; Viel, 1999)).

Regulation of NcKar9N dimerization by phosphorylation

Interestingly, the Cdk1 phosphorylation site S197 in ScKar9N, which is critical for spindle positioning, is well conserved amongst Kar9 orthologues including in NcKar9 (S190; Figure S1A). We noticed two additional putative Cdk1 phosphorylation sites (minimally S/T-P and optimally S/T-P-X-R/K (Moreno and Nurse, 1990; Nigg, 1993)) to be conserved across Kar9

orthologues, namely T202 and S229 in ScKar9 (T195 and S225 in NcKar9; Figure 3A). To the best of our knowledge, these two sites have not been studied so far.

In our NcKar9N structure, the three putative Cdk1 phosphorylation sites are located in loops H4-H5 and H5-H6 of SR2 (Figure S1). Strikingly, in the crystallographic NcKar9N dimer structure all six putative phosphorylation sites (i.e., three per NcKar9N molecule) are located in very close proximity (Figure 2A), surrounding the dimerization interface, and could thus affect dimer formation, for example, through electrostatic repulsion. To test this idea, we produced a phosphomimetic NcKar9N variant in which S190, T195 and S225 were simultaneously mutated to glutamates (NcKar9N-3E). CD analysis of NcKar9N-3E confirmed the folding integrity of this mutant (Figure S3). SEC-MALS analysis showed that NcKar9N-3E eluted at a volume of 13.3 ml with a molecular mass of 61.2 ± 0.4 kDa, at values intermediary to those obtained for the wild type protein and the dimer interface mutant (Figure 2C). Since the size, shape and single negative charge of a glutamate can only partially mimic the effect of a negatively charged phospho-serine, we anticipate that native phosphorylation inhibits Kar9 dimerization even further.

Together, these results suggest that Cdk1-dependent phosphorylation regulates the dimerization of Kar9's spectrin-repeat domain. The observation that all three Cdk1 consensus sites are highly conserved in Kar9 orthologues, despite being all located in variable loops of the protein, support the idea that all three residues are targeted by Cdk1 *in vivo*. Indeed, their vicinity to each other and their accessibility makes it unlikely that a kinase phosphorylating this area of Kar9 would discriminate them strongly from each other.

Previous studies have established that phosphorylation of S197 of ScKar9 (S190 in NcKar9N) and possibly other sites by the cyclin-dependent kinase Cdk1/Clb4 restricts ScKar9 localization to microtubules emanating from the old SPB and is key for proper spindle positioning (Liakopoulos et al., 2003; Maekawa and Schiebel, 2004; Moore and Miller, 2007). Notably, phospho-ablation mutation of S197A caused ScKar9 localization to being no longer restricted to only one of the two asters in metaphase cells (Hotz et al., 2012; Liakopoulos et al., 2003). How ScKar9 phosphorylation controls the localization and thus the function of the protein is unknown. It might help recruiting ScKar9 to the proper microtubule, as suggested by the co-localization of Cdk1/Clb4 together with ScKar9 to microtubule tips (Maekawa and Schiebel, 2004). However, since non-phosphorylated ScKar9 localizes to both sides of the spindle, ScKar9 phosphorylation might also displace the protein from microtubules emanating from the new SPB. Therefore, we decided to investigate next whether our structural findings could help address how Cdk1 controls Kar9 localization and function *in vivo*.

Functional relevance of NcKar9 dimerization and role of phosphorylation

To test the functional relevance of the observations that we made in vitro with NcKar9, we first asked whether NcKar9 could compensate for the loss of the endogenous ScKar9 protein in *S. cerevisiae* cells. Thus, we replaced the *KAR9* ORF in *S. cerevisiae* with full length *NcKAR9-mNeonGreen* or we tagged the endogenous *ScKAR9* by fusing in frame the mNeonGreen coding sequence (*ScKAR9-mNeonGreen*). *ScKAR9* is not an essential gene as long as the partially redundant dynein pathway is functional. Even in the absence of the dynein heavy chain (*dyn1Δ*), cells expressing NcKar9-mNeonGreen were growing nearly as well as the cells expressing endogenous ScKar9 (tagged or untagged; Figure 3B), indicating that NcKar9 can take over the function of the endogenous protein in *S. cerevisiae* cells. In contrast, the *dyn1Δ* mutant cells replacing ScKar9 with the dimerization deficient NcKar9-dim⁻ mutant (i.e., NcKar9-F288A/F344A) and even more with the NcKar9-3E phosphomimetic mutant protein showed significantly impaired growth (Figure 3B), suggesting that NcKar9 dimerization is needed for its function.

We then used live-cell fluorescence microscopy to investigate the effects of the dimerization and phosphomimetic mutations on NcKar9 localization and function. Co-expression of CFP-Tub1 visualized the mitotic spindle. As expected, NcKar9-mNeonGreen decorated astral microtubule plus ends similar to ScKar9-mNeonGreen, though slightly less efficiently (Figure 3C-E). By comparison, tagged NcKar9-dim⁻ and NcKar9-3E proteins displayed a clearly reduced ability to localize to plus ends. About 45% of NcKar9-dim⁻ and 60% NcKar9-3E expressing cells showed no foci, while the foci formed in the rest of the cells were of severely reduced intensities compared to NcKar9-mNeonGreen (Figure D-E). As one might predict, spindle positioning and alignment correlated well with the ability to asymmetrically recruit NcKar9 to microtubule plus ends. NcKar9 promoted positioning of the metaphase spindle to the bud neck similarly well as ScKar9, whereas the NcKar9-dim⁻ and NcKar9-3E mutant proteins failed to do so (Figure 3F-G).

Together, these results suggest that the dimerization role of NcKar9's spectrin-repeat domain observed in vitro are key to mediate proper localization of the protein to microtubule plus ends in vivo. In accordance, phosphomimetic mutations that dissociate the NcKar9 dimer in vitro displace the protein from microtubule tips in vivo.

Role of ScKar9 dimerization in spindle positioning and alignment

Next, we investigated whether ScKar9 also needs dimerization of its N-terminal domain to function. First, we examined the role of the N-terminal domain of ScKar9. To this end, we

removed it altogether and created the *ScKar9 Δ N* allele (Figure 4A). The ScKar9 Δ N protein localized to the shaft of astral microtubules, albeit weakly, and showed little enrichment at microtubules tips (Figure 4B). Most of the protein remained diffuse in the cytoplasm. Furthermore, this allele completely failed to promote the proper positioning of metaphase spindles (Figure 4B-G).

To test, whether some of these effects were due to a dimerization defects, we next replaced the N-terminal domain of Kar9 with the coiled-coil domain of the human protein ATF1 (Ciani et al., 2010), which readily dimerizes (ATF1-ScKar9 Δ N; Figure 4A). Restoration of dimerization relocalized ScKar9 Δ N from the cytoplasm to microtubules, where it reached levels above those observed for wild type ScKar9 (Figure 4B, 4D). However, microtubule localization was not sufficient for ATF1-ScKar9 Δ N to properly function in spindle positioning (Figure 4B-G). ATF1-ScKar9 Δ N decorated all cytoplasmic microtubules along their entire shaft instead of being restricted to the plus tip of only one or few microtubules emanating from the old SPB. Furthermore, as for those labelled with ScKar9 Δ N, the microtubules decorated with ATF1-ScKar9 Δ N only rarely oriented towards the bud (Figure 4E).

Thus, Kar9 dimerization is not sufficient to ensure the orientation of the ScKar9-decorated microtubules along actin cables. The failure of these microtubules to find their way to the bud in *ScKar9 Δ N* mutant cells suggests that ScKar9N may contribute to the interaction of the protein with the actin cytoskeleton, possibly through recruitment of Myo2 to microtubule tips. Together, these results indicate that while dimerization of ScKar9 indeed facilitates ScKar9 recruitment to microtubules, the N-terminal domain of ScKar9 is also required for focusing ScKar9 distribution to microtubule tips and for their proper movement towards the bud.

In order to investigate further the function of ScKar9 dimerization itself, we investigated how point mutations affecting the self-interaction of ScKar9N interfere with ScKar9 localization. Since the residues involved in dimerization are well conserved between NcKar9 and ScKar9 (Figure S1A), we mutated the ScKar9 dimer interface residues F195, F292 and L347 to alanines, generating the dimerization defective allele *ScKar9-dim*. As we observed with NcKar9, this allele was synthetically sick in combination with the *dyn1 Δ* mutation (Figure 5A), indicating that dimerization is required for ScKar9 to properly function.

Live-cell imaging indicated that the ScKar9-F195A/F292A/L347A-mNeonGreen protein localized only faintly to microtubules, in a rather symmetric manner (Figure 5C-E). As expected, this allele also affected the ability of the cells to properly align and position their metaphase spindle (Figure 5F-G). These phenotypes were indeed caused by ScKar9's deficient dimerization, since they were extensively corrected upon introducing a dimerization domain in the protein. Indeed, introducing the dimerization domain of the Gcn4 protein (O'Shea

et al., 1991) at different positions in the tail domain of the ScKar9-*dim⁻* protein (ScKar9-Gcn4-m in the middle and ScKar9-Gcn4-e in the end of the disordered tail; Figure 5B) rescued both the recruitment of the protein to microtubule tips and its asymmetric localization on spindle asters (Figure 5C-E). Furthermore, it somewhat rescued the spindle positioning and alignment defect of the dimerization mutant as well (Figure 5F-G). Thus, ScKar9 needs indeed to dimerize in order to properly decorate microtubules and function in spindle positioning.

The phosphorylation sites targeted by Cdk1 in Kar9N are also conserved and therefore we investigated the effect of mimicking constitutive phosphorylation of ScKar9. We introduced the phosphomimetic mutations S197E, T202E and S229E in ScKar9 to generate the alleles *ScKar9-S197E* and *ScKar9-S197E/T202E/S229E* (denoted *ScKar9-3E*). Consistent with phosphorylation affecting dimerization, the ScKar9-S197E-mNeonGreen and ScKar9-3E-mNeonGreen proteins failed to efficiently accumulate on astral microtubules and to localize asymmetrically to only one aster, like the dimerization-defective allele. In addition, the phosphomimetic mutant cells failed to orient aster microtubules towards the bud (Figure 6B), a phenotype that was quite prominent in these cells, although it was only weakly observed in the *ScKar9-dim⁻* mutant cells. Supporting the idea that not only S197 is phosphorylated in vivo, the *ScKar9-3E* mutant cells showed stronger phenotypes than the cells expressing ScKar9-S197E. ScKar9-3E was even less abundant on microtubules, failed to decorate the asters asymmetrically, and caused more penetrant microtubule orientation and spindle positioning phenotypes than the ScKar9-S197E protein (Figure 5G, Figure 6B). Forced dimerization of the phosphomimetic forms of ScKar9 rescued its recruitment to microtubule tips and its asymmetric localization, as for the ScKar9-*dim⁻* protein. Remarkably however, it did not rescue the alignment and spindle position defects of the mutant cells. Particularly, it did not restore the orientation of the ScKar9-3E decorated microtubules towards the bud (Figure 6B).

Based on these results and the observation that ScKar9 Δ N also failed to promote microtubule orientation towards the bud, we reasoned that ScKar9N might play a prominent role in ScKar9 interaction with Myo2 and that its phosphorylation on S197, T202 and S229 might inhibit its binding to Myo2, in addition to preventing ScKar9 dimerization. In order to test this hypothesis, we scored the recruitment of Myo2 to ScKar9-decorated microtubules. Cells expressing Myo2 tagged with GFP and ScKar9 C-terminally fused with three repeats of the red fluorophore mKate2 (ScKar9-3xmKate) were imaged by time-lapse microscopy in both the green and red fluorescence channels, and the colocalization of Myo2 signal with ScKar9 foci was assessed in cells where the ScKar9 focus entered the bud (Figure 6A, C). Such events were frequent in wild type cells and in nearly 75% of these cases some unambiguous Myo2-GFP staining clearly overlapped with the ScKar9-3xmKate signal. In contrast, cells expressing ScKar9 Δ N-3xmKate,

ATF1-ScKar9 Δ N-3xmKate and ScKar9-3E-3xmKate showed only rarely ScKar9 foci entering the bud and even these foci were only rarely overlapping with any signal from the Myo2-GFP channel (overlap observed in 8, 12 and 15 % of the cases, respectively; Figure 6A, C).

We conclude that ScKar9N has at least two key functions towards mediating proper positioning of the spindle, both of which are inhibited by phosphorylation of its Cdk1-consensus sites. On one hand it mediates ScKar9 dimerization, which is necessary for the proper recruitment of ScKar9 to the tip of a single or few microtubules at only one of the two mitotic asters. On the other hand, it contributes to Myo2-recruitment to the tip of microtubules.

DISCUSSION

In combination with our previous findings (Honnappa et al., 2009; Kumar et al., 2017; Manatschal et al., 2016), our structural studies establish that Kar9 is formed of an N-terminal domain made of three spectrin-repeat and a disordered C-terminal domain, containing the EB1-binding motifs SxIP- and LxxPTPh. The identity of the Kar9 homologues in metazoans is still a matter of debate. Based on functional conservation (i.e., capability to link microtubule plus ends with actin filaments) and a short sequence site of limited similarity, it has been initially proposed that Kar9 is related to the human tumor suppressor adenomatous polyposis coli (APC; Figure S1B), an EB1-binding and microtubule-actin crosslinking protein (Bienz, 2001). The organization of Kar9 (i.e., combination of an oligomerization domain with multiple EB1-binding sites) and its scaffolding function suggested later that Kar9 could equally well be related to the EB1-binding protein SLAIN2 (Manatschal et al., 2016). This protein is structured around an N-terminal coiled-coil domain, and a C-terminal disordered domain containing multiple SxIP- and LxxPTPh-motifs, and displays scaffolding properties similar to Kar9 (Figure S1B) (Kumar et al., 2017; Van der Vaart et al., 2011).

The spectrin repeats identified through our current structural studies are reminiscent of those present in the EB1-binding, microtubule-actin crosslinking factor (MACF/ACF7/Shot). The members of this protein family are large multidomain proteins that link growing microtubule plus ends with actin filaments in an EB1-dependent manner in metazoans (Alves-Silva et al., 2012; Kodama et al., 2003; Lee et al., 2000; Lee and Kolodziej, 2002; Wu et al., 2008). Like Kar9, the C-terminal half of MACF/ACF7/Shot consists of several spectrin-repeats and an unstructured region containing also SxIP- and LxxPTPh-motifs (Figure S1B). The roles of the spectrin repeats of MACF/ACF7/Shot are not fully understood. They might collectively function as a spacer to separate different functional domains at the N- and C-termini and provide some flexibility to the protein (Hu et al., 2016). Our data here and elsewhere (Manatschal et al., 2016) establish two key functions of the spectrin-repeat domain of Kar9: first, Kar9N recruits Myo2 to microtubule tips, possibly by directly interacting with it. Second, it mediates subunit dimerization with an affinity between Kar9 molecules in the micromolar range. Since Kar9 contains at least three binding sites for the Bim1 (EB1) dimer (Kumar et al., 2017), we anticipate that the rather weak homotypic interaction between Kar9 monomers would become functionally relevant when several copies of Kar9 and Bim1 localize together as a network to the confined space of a microtubule tip, where their local concentration is increased. Since the phenotypes, due to erasing Kar9's dimerization interface, are extensively if not fully rescued by adding a heterologous dimerization domain, the role of the spectrin repeats in Kar9 dimerization appears as a major function of Kar9N in vivo, independently of the formal

possibility that the mutated residues might also mediate interaction with other factors. Interestingly, phosphomimetic mutations in the dimerization interface did not only prevent Kar9 dimerization but also inhibited the recruitment of myosin V to microtubule tips by Kar9 and microtubule orientation towards the bud. This last defect was not rescued by forcing Kar9 dimerization. Thus, the dimerization and Kar9-Myo2 interaction interfaces might partially overlap. The notion that phosphorylation affects both types of interaction might be functionally important, contributing to coordinating the recruitment of Kar9 to microtubule tips with its transport along actin cables. For example, this might avoid futile transport of Kar9 to the bud after phosphorylation has removed it from the tip of astral microtubules.

Interestingly, the arrangement of a spectrin-repeat dimerization domain in tandem with an EB1-binding, SxIP-motif containing disordered region is also found in the spindle-microtubule crosslinking protein PRC1/Ase1, where it promotes its efficient recruitment to microtubules (Subramanian et al., 2010; Thomas et al., 2020), similar to what we observe with Kar9. We thus speculate that one of the generic functions of spectrin repeats found in several patterning +TIPs might be to mediate homo- and/or heterotypic protein-protein interactions needed to target these proteins to subsets of microtubules. Together, these considerations establish that Kar9 features several different structural elements and motifs, which are conserved in major +TIPs. They further reveal that the specific arrangement of a spectrin-repeat domain and an EB1-binding region is a hallmark of key proteins involved in the crosstalk between cytoskeletal filaments in Eukaryotes.

Our functional data further indicate that dimerization plays a central role in the efficient and stable recruitment of Kar9 to the tip of dynamic microtubules. Therefore, Kar9 binding to Bim1 is essential but not on its own sufficient for microtubule tip tracking. Some level of avidity of the Kar9 network for microtubules may be required for making the process efficient, by enabling multiple interactions between Kar9, +TIP network partners and the microtubule tip (Akhmanova and Steinmetz, 2015). We further found that the regulation of Kar9 dimerization by Cdk1-dependent phosphorylation is a conserved mechanism across budding yeasts to inhibit Kar9 interaction with microtubule tips and regulate its subcellular localization. In conclusion, the structural characterization of Kar9 has brought us closer to understand at the molecular level how budding yeast cells spatially coordinate the interaction of aster microtubules with actin filaments and how they properly orient their spindles along the mother bud axis. Whether these mechanisms can be transposed to other cell types will have to be investigated. However, one important insight provided by our study is that the avidity of interactions that a +TIP establishes with microtubule tips, increased by dimerization in the case of Kar9, is an important parameter for controlling its localization and a target of regulation by posttranslational modification. It is

likely that this requirement is relevant for patterning +TIPs in general. Therefore, dissecting the mechanisms and modes of regulation of such avidity mechanisms will be important for better understanding how cells control and pattern the interaction of microtubule tips with subcellular targets to properly position and orient larger structures such as the mitotic spindle.

ACKNOWLEDGMENTS

We are indebted to Andrea Prota for excellent support with the NcKar9N model building and refinement. X-ray data were collected at beamline X06DA of the Swiss Light Source (Paul Scherrer Institut, Villigen, Switzerland). This work was supported by a Marie Curie COFUND fellowship (to A.K.), and by grants from the Swiss National Science Foundation (31003A_166608, to M.O.S.; Sinergia CRSII5_189940, to Y.B. and M.O.S) and from SystemsX.ch (RTD-TubeX, to Y.B. and M.O.S.).

AUTHOR CONTRIBUTIONS

A.K., S.M.M., and A.-M.F. designed and performed the research, and analyzed the data. C.M. designed and performed initial experiments. Y.B. and M.O.S. designed and supervised the research, analyzed the data and wrote the manuscript with input from all authors.

DECLARATION OF INTERESTS

The authors declare no competing interests.

FIGURE LEGENDS

Figure 1. Structure of NcKar9N and surface residue conservation.

A, Overall view of the NcKar9N structure in ribbon representation. The three spectrin-repeats are color coded in blue (SR1; residues 39-152), orange (SR2; residues 153-301) and purple (SR3; residues 302-400). The N-terminal helix H1 and helix H5 of SR2 are colored in grey.

B, Side-by-side views of SR1 (blue), SR2 (orange), and SR3 (purple) of NcKar9N and SR8 (yellow) of human erythroid spectrin (PDB ID 1S35). The respective three-helix bundles in the spectrin-repeat domains are labeled as helices A, B and C. The gray segments in SR1 and SR2 of NcKar9N correspond to secondary structural elements that do not belong to the canonical spectrin-repeat fold.

C, Two views 180° apart of the surface representation of the NcKar9N structure highlighting identical (dark green) and conserved (light green) surface exposed amino acid residues. Conserved residue surface patches are highlighted with dashed circles.

See also Figure S1 and S2.

Figure 2. Structural basis of NcKar9N dimerization and phospho-regulation.

A, Overall structure of the crystallographic NcKar9N dimer displaying the largest buried surface area in the crystal. The two NcKar9N molecules are shown in ribbon representation and colored in light and dark gray, respectively. The three spectrin repeats are labeled in both NcKar9N molecules. The interface residues F288 and F344 as well as the putative Cdk1 phosphorylation sites S190, T195 and S225 are highlighted in green and blue spheres representation, respectively. The dashed box indicates the region shown in panel B.

B, Close up view of the dimer interface. Interacting residue side chains are shown in stick representation. Oxygen and nitrogen atoms are colored in red and blue, respectively; carbon atoms are in light and dark gray for chains A and B, respectively. The two residues F288 and F344 that were mutated in NcKar9N are labeled in bold and blue lettering. Selected secondary structural elements are indicated with underlined letters.

C, SEC-MALS experiments of His-NcKar9N WT (black), His-NcKar9N-F288A/F344A (red), and His-NcKar9N-3E (blue). Thick lines indicate molecular weight determinations at peaks; thin lines indicate differential refractive index elution profiles. All proteins were loaded at 50 μ M

concentration on a S200 10/300 size exclusion column equilibrated in 250 mM NaCl, 20 mM Tris-HCl at pH 7.5, 1 mM DTT.

See also Figure S3.

Figure 3. NcKar9 function in *S. cerevisiae*.

A, Sequence alignment showing conservation of Cdk1 sites between ScKar9 and NcKar9. Putatively phosphorylated serine and threonine residues are highlighted in blue; additional residues of the consensus motifs are highlighted in grey.

B, Viability of ScKar9 and NcKar9 wild type and NcKar9 mutants with *dyn1Δ*. Dissected tetratype tetrads after crosses of *kar9::kar9** (*kar9** denoting Kar9 alleles) with *dyn1Δ/kar9-wt* strains. *kar9*/dyn1Δ* double mutants are indicated by arrowheads. *kar9** is either *ScKar9-wt* (*Scwt*), *NcKar9-wt* or *NcKar9-mutant*.

C, Micrographs of metaphase *S. cerevisiae* cells with CFP-Tub1 (red) labelling mitotic spindles and *kar9::kar9*-mNeonGreen* (green). Scale bar 3 μ m.

D, Quantification of Kar9 asymmetry on metaphase spindles in CFP-Tub1 expressing *kar9::kar9*-mNeonGreen* strains (frequency over all analyzed cells with Wilson/Brown 95% confidence intervals). Cells with a Kar9 focus on only one side of the spindle are considered asymmetric. If there is a focus on one side and only little intensity on the other side, it is considered weakly symmetric. If there are equally intense foci on both sides, it is considered symmetric. If there are no foci visible at all, it is considered as no focus. Significance tests compare frequency of full asymmetry by two-proportion z-test. Significance tests compare frequency of full asymmetry by two-proportion z-test. Minimum 172 cells from 3 clones analyzed for each allele, same for all panels. Detailed numbers are provided in Table S1. Significance levels from here onwards: $p > 0.05$, ns; $p < 0.05$, *; $p < 0.01$, **; $p < 0.001$, ***; $p < 0.0001$, ****.

E, Quantification of Kar9 focus intensity in CFP-Tub1 expressing *kar9::kar9*-mNeonGreen* strains normalized to ScKar9-wt-mNeonGreen, logarithmic scale. Intensities are background (medium) subtracted average maximum intensity values over a time course per cell. Lines are median with interquartile range over pooled values of all analyzed cells. Significance levels calculated by Welch corrected t-test.

F, Quantification of metaphase spindle alignment relative to the bud neck in CFP-Tub1 expressing *kar9::kar9** strains compared to *kar9Δ* (frequency over all analyzed cells with Wilson/Brown 95% confidence intervals). If the extended axis of a spindle passes the bud

neck, the spindle is considered aligned, if not it is considered misaligned; in case of uncertainty it is considered ambiguous. Significance tests compare frequency of correct alignment by two-proportion z-test.

G, Metaphase relative spindle position (RSP) of CFP-Tub1 expressing *kar9::Nckar9* strains compared to *ScKar9-wt* and *kar9Δ*. Plotted values are distance from the middle of the spindle (A) to the center of the bud neck (B) normalized to the length of the mother compartment (BC) for each cell. Lines are median with interquartile range over pooled values of all analyzed cells. Significance levels calculated by Welch corrected t-test.

Figure 4. Role of Kar9N in vivo

A, Illustrations of ScKar9-wt, ScKar9ΔN and ATF1-ScKar9ΔN constructs

B, Micrographs of metaphase *S. cerevisiae* cells with CFP-Tub1 (red) labelling mitotic spindles and *kar9::kar9*-mNeonGreen* (green). Scale bar 3 μm.

C, Quantification of ScKar9 asymmetry on metaphase spindles in CFP-Tub1 expressing *kar9::kar9*-mNeonGreen* strains as described in Figure 3D. Minimum 52 cells from 2 clones analyzed for each allele, same for all panels.

D, Quantification of ScKar9 focus intensity in CFP-Tub1 expressing *kar9::kar9*-mNeonGreen* strains normalized to ScKar9-wt-mNeonGreen; logarithmic scale, as previously described in Figure 3E.

E, Quantification of ScKar9 focus orientation towards the bud in metaphase, frequency over all analyzed cells with Wilson/Brown 95% confidence intervals. If a line through a spindle pole and associated ScKar9 focus passes the bud neck, the focus is considered oriented; otherwise misoriented. Significance tests compare frequency of correct orientation by two proportion z-test.

F, Quantification of metaphase spindle alignment relative to the bud neck in CFP-Tub1 expressing *kar9::kar9** strains compared to *kar9Δ* (*kar9Δ* data taken from Figure 3F), as previously described in Figure 3F.

G, Metaphase spindle position of CFP-Tub1 expressing *kar9::Sckar9-mNeonGreen* strains compared to *kar9Δ* (data taken from Figure 3G), as previously described in Figure 3G.

Figure 5. Effect of ScKar9 dimerization and phosphomimetic mutations in vivo.

A, Viability of ScKar9-wt and mutants with *dyn1Δ*. Dissected tetratype tetrads after crosses of *kar9::kar9** with *dyn1Δ/kar9-wt* strains. *kar9*/dyn1Δ* double mutants are indicated by arrowheads. *kar9** is either *Sckar9-wt* or *Sckar9-mutant*.

B, Illustrations of constructs rescuing dimerization of ScKar9 dimer and phosphomimetic mutants.

C, Micrographs of metaphase *S. cerevisiae* cells with CFP-Tub1 (red) labelling mitotic spindles and *kar9::kar9*-mNeonGreen* (green). Scale bar 3 μm.

D, Quantification of ScKar9 asymmetry on metaphase spindles in CFP-Tub1 expressing *kar9::kar9*-mNeonGreen* strains, as previously described in Figure 3D. Minimum 113 cells from 3 clones analyzed for each allele, same for all panels.

E, Quantification of ScKar9 focus intensity in CFP-Tub1 expressing *kar9::kar9*-mNeonGreen* strains normalized to ScKar9-wt-mNeonGreen; logarithmic scale, as previously described in Figure 3E.

F, Quantification of metaphase spindle alignment relative to the bud neck in CFP-Tub1 expressing *kar9::kar9** strains compared to *kar9Δ* (*kar9Δ* data taken from Figure 3F), as previously described in Figure 3F.

G, Metaphase spindle position of CFP-Tub1 expressing *kar9::Sckar9-mNeonGreen* strains compared to *kar9Δ* (same data as in Figure 3G), as previously described in Figure 3G.

Figure 6. Effect of ScKar9N removal and phosphorylation on ScKar9-Myo2 interaction.

A, Time series of micrographs displaying ScKar9-Myo2 colocalization (ScKar9-wt) or lack of colocalization (ScKar9ΔN). Scale bar 3 μm.

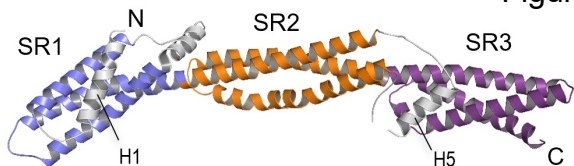
B, Quantification of ScKar9 focus orientation towards the bud in metaphase, as previously described in Figure 4E. Minimum 113 cells from 3 clones analyzed for each allele, same for all panels.

C, Quantification of ScKar9-Myo2 colocalization, frequency over all analyzed cells with Wilson/Brown 95% confidence intervals. If the ScKar9-3xmKate focus colocalizes (in x, y and z) with focalized Myo2-GFP intensity in at least 2 out of 5 time-frames, it is considered as colocalized; otherwise not colocalized. If there is colocalization involving diffuse signal in either channel or large Myo2 patches only partially overlapping with ScKar9 signal, it is considered as ambiguous colocalization. Significance tests compare frequency of unambiguous

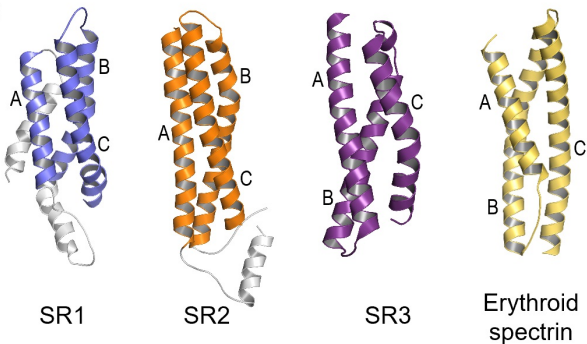
colocalization by two proportion z-test. Minimum 42 cells from 2 clones (except only 1 clone for WT) analyzed for each allele, same for all panels.

Figure 1

A



B



C

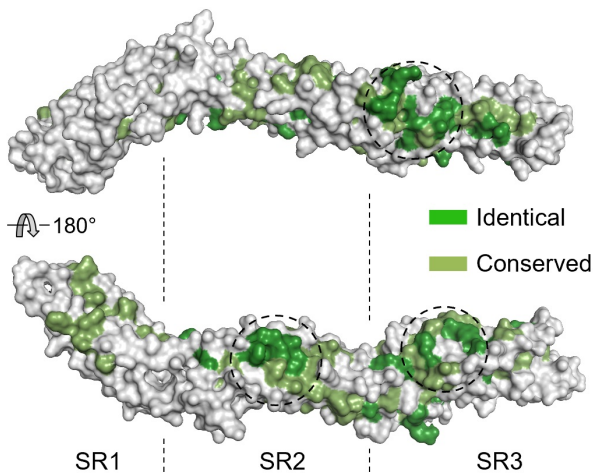
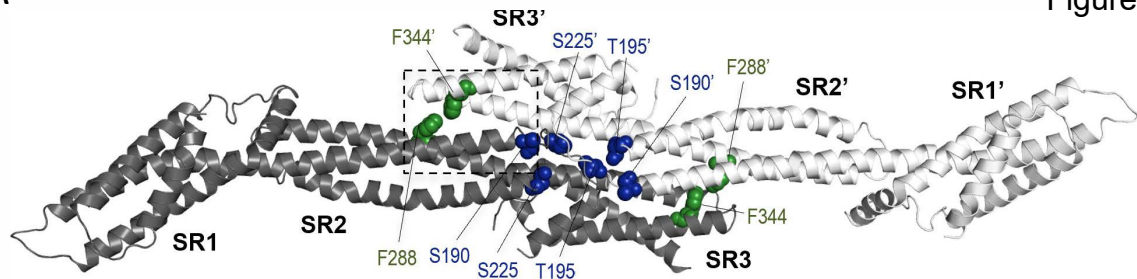
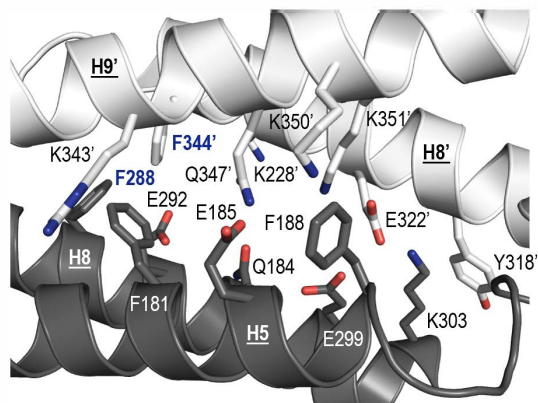


Figure 2

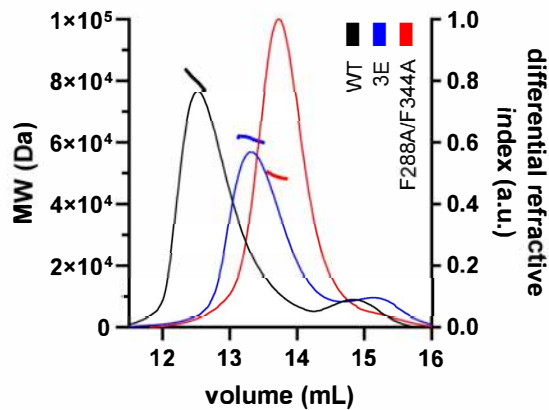
A



B



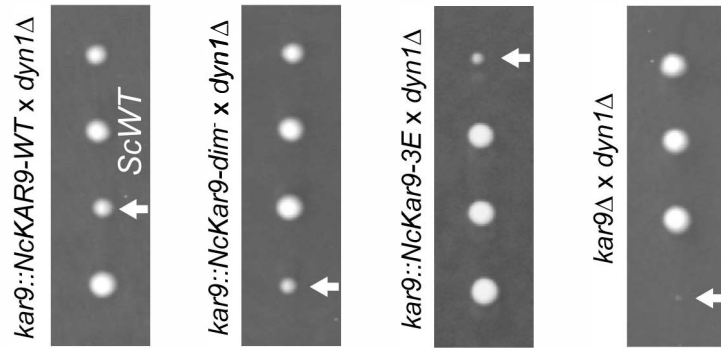
C



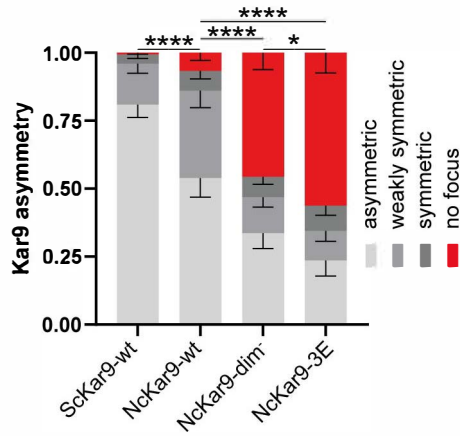
A

N.castellii 183 IQELKFSS **S** **P**VRH **T**PNFTLDQLIKLLSSNNNTTDTMEPKIPNF **S** **P**VEESLSR 233
S.cerevisiae 190 IQEERFAS **P**IRH **T**PSFTLEQLVKLLGTH - - -TETTEPKVPKF **S** **P**AEIDILSR 237

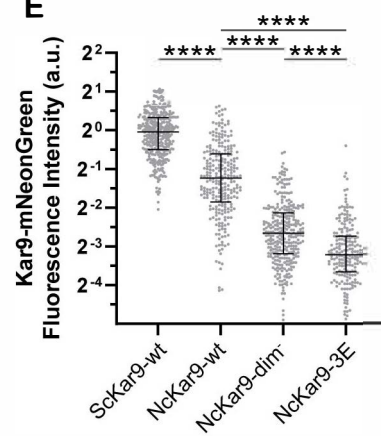
B



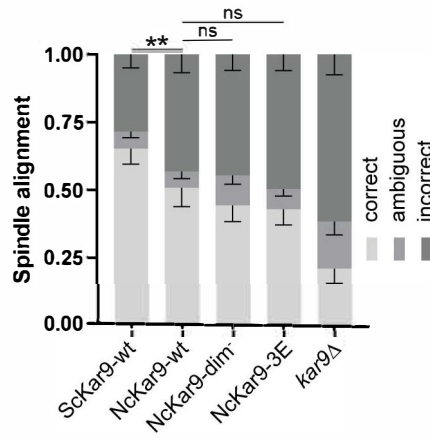
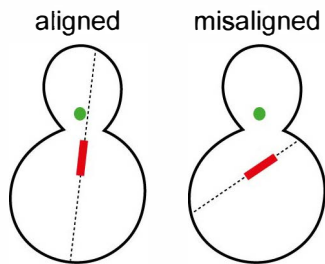
D



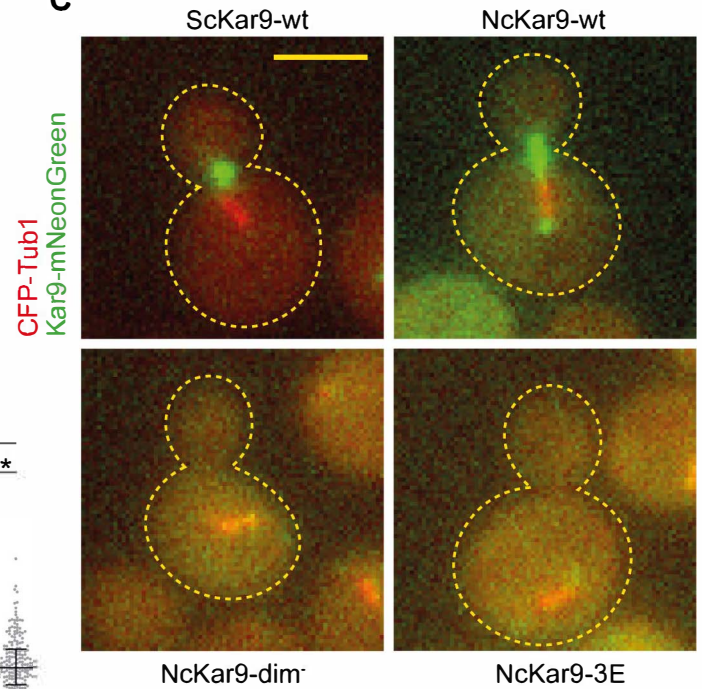
E



F



C



G

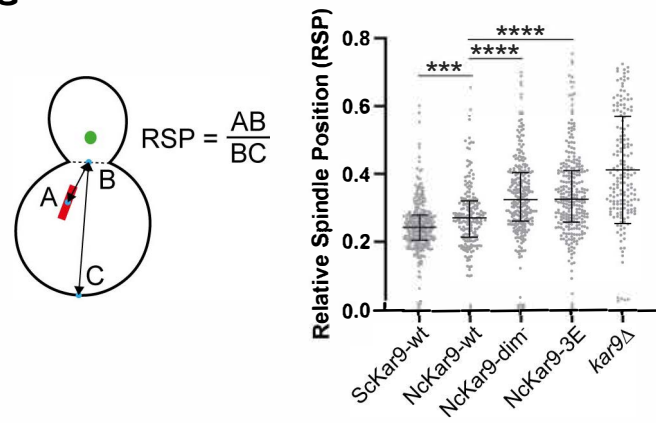


Figure 4

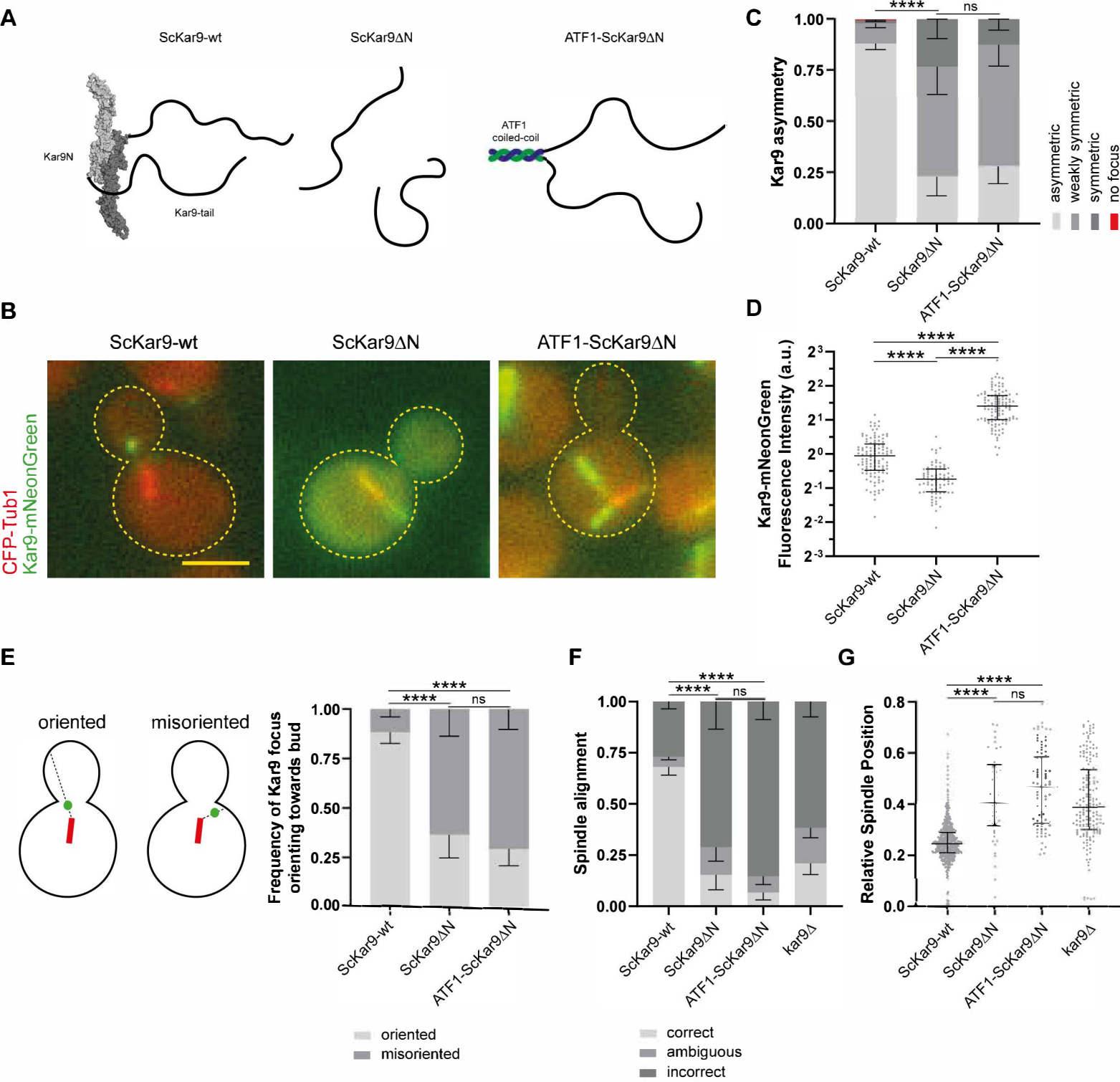
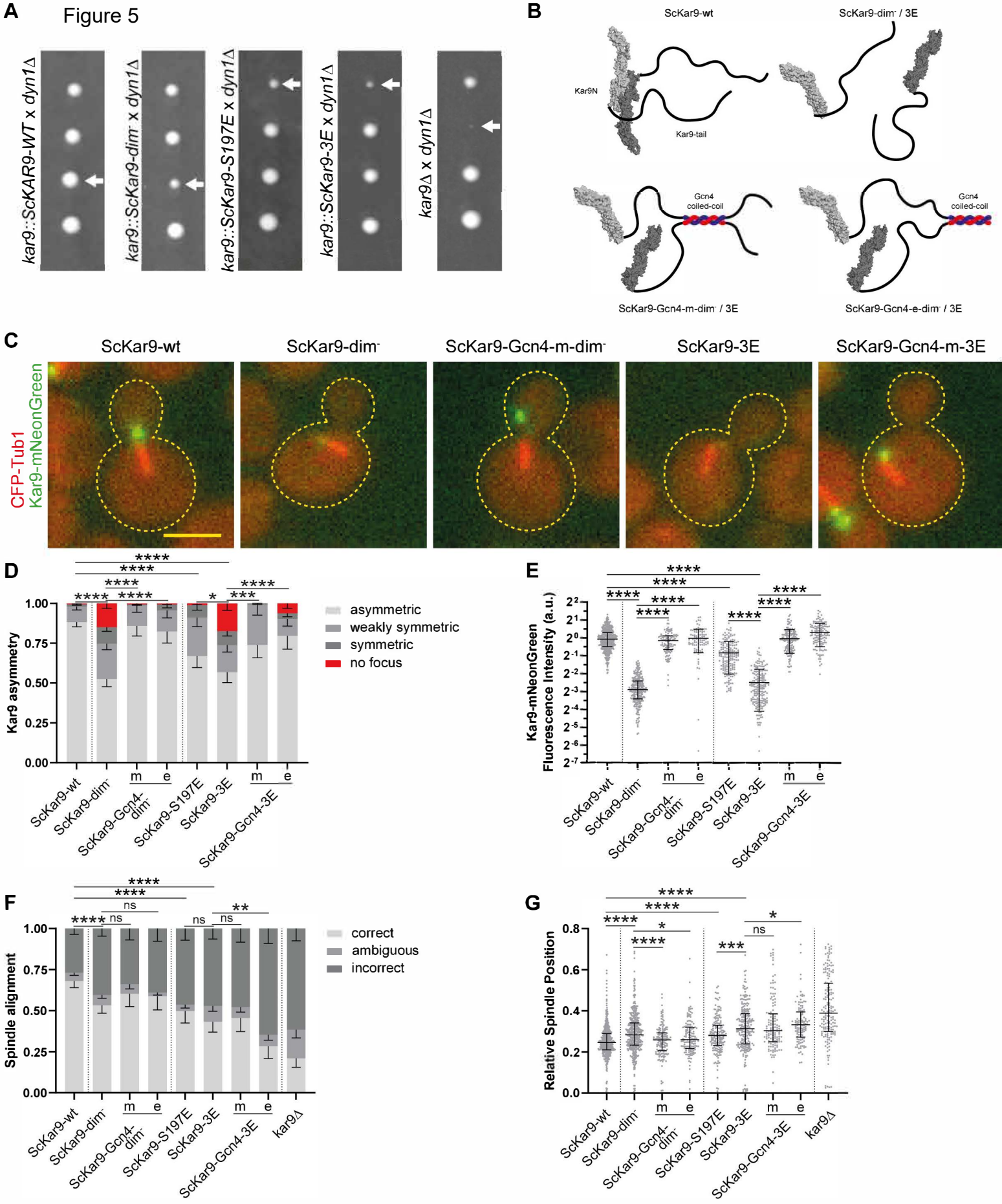
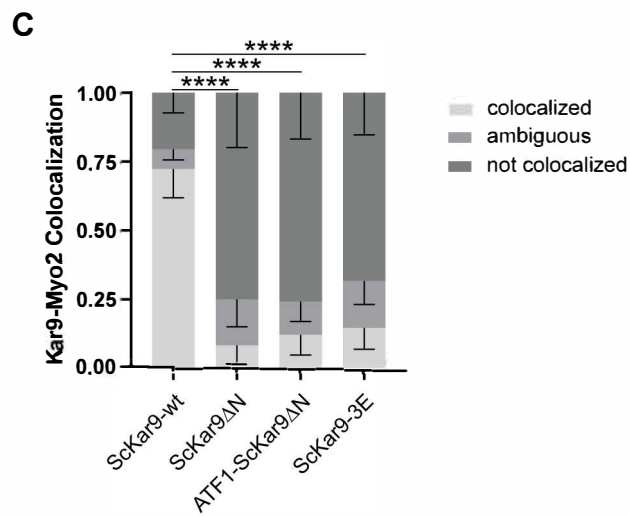
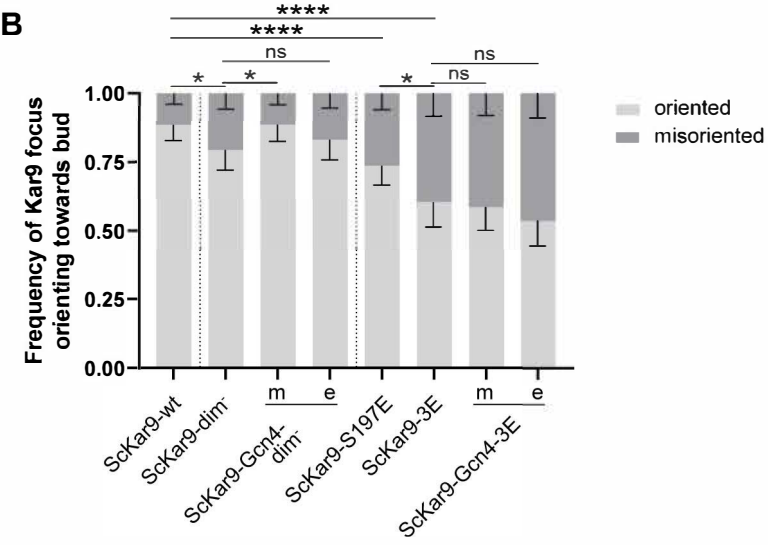
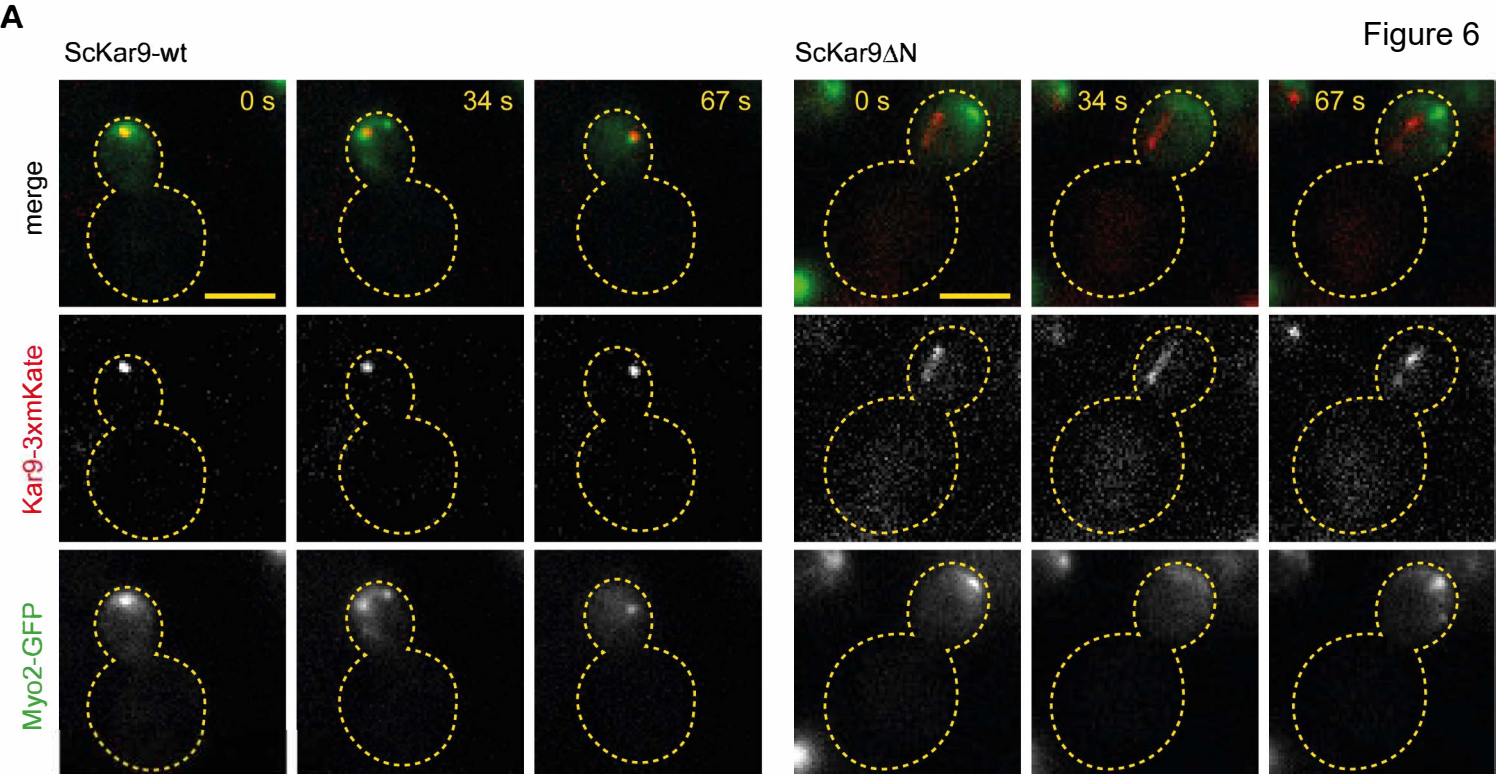


Figure 5





TABLES

Table 1. X-ray data collection and refinement statistics

	Native NcKar9N	SeMet λ -peak NcKar9N
Data collection		
Space group	P4 ₁	P4 ₁
Cell dimensions		
<i>a</i> , <i>b</i> , <i>c</i> (Å)	125.6, 125.6, 165.2	126.5, 126.5, 166.9
Resolution (Å)	46.8-3.3 (3.4-3.3)	42.2-3.5 (3.59-3.50)
R _{meas} (%)	9.8 (195.0)	22.9 (474.8)
<i>I</i> / σ <i>I</i>	16.4 (1.47)	19.5 (5.0)
CChalf	99.9 (51.0)	100 (43.6)
Completeness (%)	98.6 (91.8)	99.7 (100)
Redundancy	12.3 (6.4)	13.2 (4.6)
Refinement		
Resolution (Å)	46.8-3.3	
No. unique reflections	38506	
<i>R</i> _{work} / <i>R</i> _{free}	26.3 / 28.9	
No. atoms		
Protein	5948	
Water	n.a.	
Average <i>B</i> -factors (Å ²)		
Protein	160.0	
Water	n.a.	

Wilson <i>B</i> -factor	141.5	
R.m.s. deviations		
Bond lengths (Å)	0.002	
Bond angles (°)	1.2	
Ramachandran statistics		
Favored regions (%)	95.0	
Allowed regions (%)	5.0	
Outliers (%)	0.0	

Data were collected from a single crystal. Values in parentheses are for highest-resolution shell.

STAR★METHODS

RESOURCE AVAILABILITY

Lead contact

Further information and requests for resources and reagents should be directed to and will be fulfilled by the lead contact, Michel O. Steinmetz (michel.steinmetz@psi.ch).

Materials availability

Materials generated in this study can be made available upon request to the lead contact.

Data and code availability

Data availability: Atomic coordinates and structure factors for NcKar9N have been deposited in the RCSB Protein Data Bank (PDB) under accession number 7AG9.

Code availability: This paper does not report original code.

Post-publication availability of data and code: Any additional information required to reanalyze the data reported in this paper is available from the lead contact upon request.

EXPERIMENTAL MODEL AND SUBJECT DETAILS

Bacterial cell culture

Cloning was performed in *E.coli* DH5alpha or MACH1 cells, protein expressing in *E.coli* BL21 (DE3) cells. Transformed cells were grown in LB containing the appropriate antibiotics at 37°C. Protein expression was induced in cultures around OD600 of 0.6 by addition of 0.75 mM IPTG at 20°C overnight.

Yeast cell culture

S. cerevisiae (S288C) transformants were grown on YPD antibiotic or synthetic amino acid dropout selection agar plates at 25 or 30°C. Single clones were frozen in YPD glycerol stocks at -80°C for further usage. For microscopy experiments, cells were first thawed on YPD agar plates and then grown overnight in synthetic medium lacking tryptophan at 25°C. All yeast strains are S288C background with the genotype: *ura3-52 his3Δ200 leu2 lys2-801 ADE2*. All yeast strains used in this study are listed in the accompanying Key Resources Table.

METHOD DETAILS

Plasmid construction and protein preparation

The N-terminal domain (residues 1-410) of *N. castellii* Kar9 (wild type or mutants) was N-terminally tagged with 6x-histidine residues (6xHis-NcKar9N) and cloned into the pET-based expression vectors pSPCm-2 and NSKn-1 (Olieric et al., 2010). Sequence verified plasmids were transformed into BL21(DE3) *E. coli* cells for protein expression. To produce the proteins, liquid cultures were grown in LB media containing the appropriate antibiotic to an OD600 of 0.6. Expression was induced by the addition of 0.75 mM isopropyl- β -D-thiogalactoside (IPTG). Induced cells were further incubated overnight at 20°C. Selenomethionine labeled NcKar9N samples were expressed in culture media supplemented with 1x selenomethionine as described in the manufacturer's protocol (Molecular Dimensions).

Cells were lysed using the sonication method or Microfluidics Microfluidizer® and cleared by centrifugation. Cleared cell lysates were filtered using a 0.45 μ M filter. Affinity purification of His-tagged NcKar9N variants was carried out at 4°C on Ni²⁺-Sepharose columns (Cytiva) according to the manufacturer's instructions. For crystallization experiments, the hexa-His tag of wild type NcKar9N was enzymatically cleaved off by precision protease treatment. All protein samples were further applied on a HiLoad Superdex 75 or 200 size exclusion chromatography column (Cytiva) pre-equilibrated in 20 mM Tris-HCl, pH 7.5, supplemented with 500 mM NaCl. The purity of recombinant proteins was confirmed by Coomassie-stained 12% SDS-PAGE. The identities of the proteins were assessed by mass spectral analyses. Exact concentrations of protein solutions were determined by absorbance at 280 nm.

Biophysical characterization

Size exclusion chromatography followed by multi-angle light scattering (SEC-MALS) experiments were performed in 20 mM Tris-HCl, pH 7.5, 250 mM NaCl, 1 mM DTT using a S200 10/300 analytical size exclusion chromatography column (GE Healthcare) connected in-line to mini-DAWN TREOS light scattering and Optilab T-rEX refractive index detectors (Wyatt Technology). 30 μ l of His-NcKar9N variants at a concentration of 50 μ M were injected for each run onto the SEC column. The Zimm model was chosen for data fitting, which was performed in the ASTRA 6 software provided with the instrument.

Circular dichroism (CD) spectra of protein samples were recorded at 20°C and at a protein concentration of 0.2 mg/ml in 20 mM Tris-HCl, pH 7.5, supplemented with 150 mM NaCl and 1 mM DTT using a Chirascan spectropolarimeter (Applied Photophysics) and a cuvette of 0.05 cm path length. Thermal unfolding profiles between 20 and 80 °C were recorded by increasing the temperature at a ramping rate of 1 °C/min monitoring the CD signal at 222 nm. Midpoints

of thermal unfolding profiles were determined using the Global3 program (Applied Photophysics).

X-ray data collection, structure solution, model refinement, and model validation

NcKar9N (0.2 mM) samples were crystallized using the sitting drop vapor diffusion method at 20 °C by mixing equal volumes of the protein and reservoir solution. Crystals were grown with a reservoir solution consisting of 250 mM gamma amino butyric acid (GABA). Single wavelength and anomalous diffraction datasets were collected at 100 K to 3.3 Å and 3.5 Å resolutions, respectively, at beamlines X06DA and X06SA at the Swiss Light Source (Villigen PSI, Switzerland). The crystals belonged to space group P41 and contained two molecules in their asymmetric unit.

Diffraction data were indexed, integrated and scaled using the XDS program (Kabsch, 2010). The NcKar9N structure was solved by identifying the labeled methionine sites using AUTOSOL in the program PHENIX (Adams et al., 2010). Iterative cycles of manual model building were performed in COOT (Emsley and Cowtan, 2004) and subsequent refinements were done using restrained refinements in REFMAC5 of the CCP4 suite (Collaborative Computational Project, 1994) to improve the phases. Inspection of the resulting FO–FC and 2FO–FC maps displayed densities for the NcKar9N segment 19 to 404 and 15 to 400 of chain A and B, respectively. Refinement was carried out until convergence. TLS (Translation, Libration and Screw) restraints were included for the final cycles of the refinement. The domain definitions were determined using the TLS Motion Determination server (Painter and Merritt, 2006). The geometry of the final refined models was validated with PROCHECK (Laskowski et al., 1993).

Figures were prepared using the program PyMOL (The PyMOL Molecular Graphics System, Schrödinger, LLC). The details of the data collection and refinement statistics are given in Table 1. Buried surface areas of crystallographic NcKar9N dimers were determined with PISA (Krissinel and Henrick, 2007).

Yeast strain generation

To create ScKar9-mNeonGreen, we have C-terminally tagged the endogenous Kar9 by amplifying the mNeonGreen:NatNT2 cassette with primers containing 30 bp homology to the Kar9 locus (the forward primer with homology to the 30 bp in Kar9 immediately upstream from the stop codon and the reverse primer with homology to the 30 bp downstream the stop codon of the endogenous Kar9 locus). Yeast strains bearing the Kar9 mutant alleles were created by the simultaneous recombination at the endogenous locus of 2 to 4 adjacent fragments. The parental strain for creating all the Kar9 mutant alleles had the Kar9 ORF deleted with the His3 auxotrophic marker (*kar9::HIS3*). Multiple fragment integration at the locus was performed by amplifying fragments with 50-60 bp of homology to their immediate neighboring fragment or to

the Kar9 locus (first fragment with homology to the promoter region and the last fragment with homology to the terminator region) and by their co-transformation in yeast. Their correct integration was confirmed by PCR and sequencing.

Since C-terminal GFP tags on Myo2 appeared to prevent its efficient function in the Kar9 pathway, Myo2 was tagged internally between amino acids 998 and 999 in the coiled-coil as described by (Gauss R, 2004) using their plasmid pOM40. Myo2-(998)-GFP appeared hyperpolarized, potentially due to lack of head-to-tail regulation previously described by (Donovan and Bretscher, 2015), but showed no defects in Kar9 pathway function.

All yeast strains used in this study are listed in the accompanying Key Resources Table.

Fluorescent microscopy

Strains were exponentially grown in synthetic medium lacking tryptophan, harvested by 1.5 min centrifugation at 600 g and imaged on microscopy slides with a Personal DeltaVision Microscope (Cytiva). For all phenotypes except Kar9-Myo2 colocalization, movies with 10 time points separated by 13 s and z-stacks of 17 layers separated by 0.3 μm in all relevant fluorescent channels were acquired and analyzed in Fiji (Schindelin et al., 2012). Spindle alignment, relative spindle position, Kar9 focus orientation and Kar9 asymmetry were determined in a single time point on sum projections of the 7 most in focus layers. Kar9 intensities were measured as the average max intensity per cell over 9 time points (time points 2-10) on max projections of all 17 layers. For Kar9-Myo2 colocalization, movies with 5 time points separated by 34 s and z-stacks of 17 layers separated by 0.3 μm in GFP and mCherry channels (changing wavelength before z). Colocalization was analyzed in individual slices.

QUANTIFICATION AND STATISTICAL ANALYSIS

Information on quantification and statistical analysis are provided in the figure legends. Minimal numbers of analyzed cells and clones are also provided in the figure legends; exact numbers are reported in Table S1. Calculations (background subtraction, normalization ratios and numbers for nominal data) were performed in Microsoft Excel 16. Plots were generated with GraphPad Prism 9. Welch's t-test calculations on continuous data (spindle position, fluorescence intensity) were performed in GraphPad Prism 9; two-proportion z-test for nominal data (Kar9 asymmetry, spindle alignment, Kar9 focus orientation, Kar9-Myo2 colocalization) was manually calculated in Microsoft Excel 16.

REFERENCES

- Adams, P.D., Afonine, P.V., Bunkoczi, G., Chen, V.B., Davis, I.W., Echols, N., Headd, J.J., Hung, L.W., Kapral, G.J., Grosse-Kunstleve, R.W., *et al.* (2010). PHENIX: a comprehensive Python-based system for macromolecular structure solution. *Acta Crystallogr DBiolCrystallogr* 66, 213-221.
- Akhmanova, A., and Steinmetz, M.O. (2008). Tracking the ends: a dynamic protein network controls the fate of microtubule tips. *NatRevMolCell Biol* 9, 309-322.
- Akhmanova, A., and Steinmetz, M.O. (2015). Control of microtubule organization and dynamics: two ends in the limelight. *NatRevMolCell Biol* 16, 711-726.
- Alves-Silva, J., Sanchez-Soriano, N., Beaven, R., Klein, M., Parkin, J., Millard, T.H., Bellen, H.J., Venken, K.J., Ballestrem, C., Kammerer, R.A., *et al.* (2012). Spectraplakins promote microtubule-mediated axonal growth by functioning as structural microtubule-associated proteins and EB1-dependent +TIPs (tip interacting proteins). *J Neurosci* 32, 9143-9158.
- Barr, F.A., and Gruneberg, U. (2007). Cytokinesis: placing and making the final cut. *Cell* 131, 847-860.
- Bienz, M. (2001). Spindles cotton on to junctions, APC and EB1. *NatCell Biol* 3, E67-E68.
- Ciani, B., Bjelic, S., Honnappa, S., Jawhari, H., Jaussi, R., Payapilly, A., Jowitt, T., Steinmetz, M.O., and Kammerer, R.A. (2010). Molecular basis of coiled-coil oligomerization-state specificity. *ProcNatlAcadSciUSA* 107, 19850-19855.
- Collaborative Computational Project, N. (1994). The CCP4 suite: programs for protein crystallography. *Acta Crystallogr DBiolCrystallogr* 50, 760-763.
- D'Avino, P.P., Giansanti, M.G., and Petronczki, M. (2015). Cytokinesis in animal cells. *Cold Spring Harb Perspect Biol* 7, a015834.
- Djinovic-Carugo, K., Gautel, M., Yläanne, J., and Young, P. (2002). The spectrin repeat: a structural platform for cytoskeletal protein assemblies. *FEBS Lett* 513, 119-123.
- Donovan, K.W., and Bretscher, A. (2015). Head-to-tail regulation is critical for the in vivo function of myosin V. *J Cell Biol* 209, 359-365.
- Emsley, P., and Cowtan, K. (2004). Coot: model-building tools for molecular graphics. *Acta Crystallogr DBiolCrystallogr* 60, 2126-2132.

Gauss R, T.M., Sommer T, Spang A (2004). New modules for the repeated internal and N-terminal epitope tagging of genes in *Saccharomyces cerevisiae*. *Yeast*.

Honnappa, S., Gouveia, S.M., Weisbrich, A., Damberger, F.F., Bhavesh, N.S., Jawhari, H., Grigoriev, I., van Rijssel, F.J., Buey, R.M., Lawera, A., *et al.* (2009). An EB1-binding motif acts as a microtubule tip localization signal. *Cell* **138**, 366-376.

Hotz, M., Leisner, C., Chen, D., Manatschal, C., Wegleiter, T., Ouellet, J., Lindstrom, D., Gottschling, D.E., Vogel, J., and Barral, Y. (2012). Spindle pole bodies exploit the mitotic exit network in metaphase to drive their age-dependent segregation. *Cell* **148**, 958-972.

Hu, L., Su, P., Li, R., Yin, C., Zhang, Y., Shang, P., Yang, T., and Qian, A. (2016). Isoforms, structures, and functions of versatile spectraplakins MACF1. *BMB Rep* **49**, 37-44.

Hwang, E., Kusch, J., Barral, Y., and Huffaker, T.C. (2003). Spindle orientation in *Saccharomyces cerevisiae* depends on the transport of microtubule ends along polarized actin cables. *J Cell Biol* **161**, 483-488.

Jiang, W., Jimenez, G., Wells, N.J., Hope, T.J., Wahl, G.M., Hunter, T., and Fukunaga, R. (1998). PRC1: a human mitotic spindle-associated CDK substrate protein required for cytokinesis. *Mol Cell* **2**, 877-885.

Kabsch, W. (2010). XDS. *Acta Crystallogr DBiolCrystallogr* **66**, 125-132.

Kodama, A., Karakesisoglou, I., Wong, E., Vaezi, A., and Fuchs, E. (2003). ACF7: an essential integrator of microtubule dynamics. *Cell* **115**, 343-354.

Korinek, W.S., Copeland, M.J., Chaudhuri, A., and Chant, J. (2000). Molecular linkage underlying microtubule orientation toward cortical sites in yeast. *Science* **287**, 2257-2259.

Krissinel, E., and Henrick, K. (2007). Inference of macromolecular assemblies from crystalline state. *J Mol Biol* **372**, 774-797.

Kumar, A., Manatschal, C., Rai, A., Grigoriev, I., Degen, M.S., Jaussi, R., Kretzschmar, I., Prota, A.E., Volkmer, R., Kammerer, R.A., *et al.* (2017). Short Linear Sequence Motif LxxPTPh Targets Diverse Proteins to Growing Microtubule Ends. *Structure* **25**, 924-932.

Kusch, J., Liakopoulos, D., and Barral, Y. (2003). Spindle asymmetry: a compass for the cell. *Trends Cell Biol* **13**, 562-569.

Kusch, J., Meyer, A., Snyder, M.P., and Barral, Y. (2002). Microtubule capture by the cleavage apparatus is required for proper spindle positioning in yeast. *Genes Dev* **16**, 1627-1639.

Laskowski, R.A., MacArthur, M.W., Moss, D.S., and Thornton, J.M. (1993). PROCHECK: a program to check the stereochemical quality of protein structures. *J Appl Cryst* **26**, 283-291.

- Lee, S., Harris, K.L., Whittington, P.M., and Kolodziej, P.A. (2000). short stop is allelic to kakapo, and encodes rod-like cytoskeletal-associated proteins required for axon extension. *J Neurosci* 20, 1096-1108.
- Lee, S., and Kolodziej, P.A. (2002). Short Stop provides an essential link between F-actin and microtubules during axon extension. *Development* 129, 1195-1204.
- Lengefeld, J., Hotz, M., Rollins, M., Baetz, K., and Barral, Y. (2017). Budding yeast Wee1 distinguishes spindle pole bodies to guide their pattern of age-dependent segregation. *Nat Cell Biol* 19, 941-951.
- Liakopoulos, D., Kusch, J., Grava, S., Vogel, J., and Barral, Y. (2003). Asymmetric loading of Kar9 onto spindle poles and microtubules ensures proper spindle alignment. *Cell* 112, 561-574.
- Liem, R.K. (2016). Cytoskeletal Integrators: The Spectrin Superfamily. *Cold Spring Harb Perspect Biol* 8.
- Maekawa, H., and Schiebel, E. (2004). Cdk1-Clb4 controls the interaction of astral microtubule plus ends with subdomains of the daughter cell cortex. *Genes Dev* 18, 1709-1724.
- Maekawa, H., Usui, T., Knop, M., and Schiebel, E. (2003). Yeast Cdk1 translocates to the plus end of cytoplasmic microtubules to regulate bud cortex interactions. *EMBO J* 22, 438-449.
- Manatschal, C., Farcas, A.M., Degen, M.S., Bayer, M., Kumar, A., Landgraf, C., Volkmer, R., Barral, Y., and Steinmetz, M.O. (2016). Molecular basis of Kar9-Bim1 complex function during mating and spindle positioning. *Mol Biol Cell* 27, 3729-3745.
- McNally, F.J. (2013). Mechanisms of spindle positioning. *J Cell Biol* 200, 131-140.
- Miller, R.K., and Rose, M.D. (1998). Kar9p is a novel cortical protein required for cytoplasmic microtubule orientation in yeast. *JCell Biol* 140, 377-390.
- Moore, J.K., and Miller, R.K. (2007). The cyclin-dependent kinase Cdc28p regulates multiple aspects of Kar9p function in yeast. *MolBiolCell* 18, 1187-1202.
- Moreno, S., and Nurse, P. (1990). Substrates for p34cdc2: in vivo veritas? *Cell* 61, 549-551.
- Nelson, S., and Näthke, I.S. (2013). Interactions and functions of the adenomatous polyposis coli (APC) protein at a glance. *J Cell Sci* 126, 873-877.
- Nigg, E.A. (1993). Cellular substrates of p34(cdc2) and its companion cyclin-dependent kinases. *Trends Cell Biol* 3, 296-301.

- O'Shea, E.K., Klemm, J.D., Kim, P.S., and Alber, T. (1991). X-ray structure of the GCN4 leucine zipper, a two-stranded, parallel coiled coil. *Science* 254, 539-544.
- Olieric, N., Kuchen, M., Wagen, S., Sauter, M., Crone, S., Edmondson, S., Frey, D., Ostermeier, C., Steinmetz, M.O., and Jaussi, R. (2010). Automated seamless DNA co-transformation cloning with direct expression vectors applying positive or negative insert selection. *BMC Biotechnol* 10, 56.
- Painter, J., and Merritt, E.A. (2006). TLSMD web server for the generation of multi-group TLS models. *J Appl Cryst* 39, 109-111.
- Pellman, D., Bagget, M., Tu, Y.H., Fink, G.R., and Tu, H. (1995). Two microtubule-associated proteins required for anaphase spindle movement in *Saccharomyces cerevisiae*. *J Cell Biol* 130, 1373-1385.
- Pereira, G., Höfken, T., Grindlay, J., Manson, C., and Schiebel, E. (2000). The Bub2p spindle checkpoint links nuclear migration with mitotic exit. *Mol Cell* 6, 1-10.
- Schindelin, J., Arganda-Carreras, I., Frise, E., Kaynig, V., Longair, M., Pietzsch, T., Preibisch, S., Rueden, C., Saalfeld, S., Schmid, B., *et al.* (2012). Fiji: an open-source platform for biological-image analysis. *Nat Methods* 9, 676-682.
- Sonnenberg, A., and Liem, R.K. (2007). Plakins in development and disease. *Exp Cell Res* 313, 2189-2203.
- Subramanian, R., Wilson-Kubalek, E.M., Arthur, C.P., Bick, M.J., Campbell, E.A., Darst, S.A., Milligan, R.A., and Kapoor, T.M. (2010). Insights into antiparallel microtubule crosslinking by PRC1, a conserved nonmotor microtubule binding protein. *Cell* 142, 433-443.
- Thomas, E.C., Ismael, A., and Moore, J.K. (2020). Ase1 domains dynamically slow anaphase spindle elongation and recruit Bim1 to the midzone. *Mol Biol Cell*, mbcE20070493T.
- van der Vaart, B., Franker, M.A., Kuijpers, M., Hua, S., Bouchet, B.P., Jiang, K., Grigoriev, I., Hoogenraad, C.C., and Akhmanova, A. (2012). Microtubule plus-end tracking proteins SLAIN1/2 and ch-TOG promote axonal development. *J Neurosci* 32, 14722-14728.
- Van der Vaart, B., Manatschal, C., Grigoriev, I., Olieric, V., Gouveia, S.M., Bjelic, S., Demmers, J., Vorobjev, I., Hoogenraad, C.C., Steinmetz, M.O., *et al.* (2011). SLAIN2 links microtubule plus end-tracking proteins and controls microtubule growth in interphase. *J Cell Biol* 193, 1083-1099.
- Viel, A. (1999). Alpha-actinin and spectrin structures: an unfolding family story. *FEBS Lett* 460, 391-394.

Wu, X., Kodama, A., and Fuchs, E. (2008). ACF7 regulates cytoskeletal-focal adhesion dynamics and migration and has ATPase activity. *Cell* 135, 137-148.

Yin, H., Pruyne, D., Huffaker, T.C., and Bretscher, A. (2000). Myosin V orientates the mitotic spindle in yeast. *Nature* 406, 1013-1015.

KEY RESOURCES TABLE

REAGENT or RESOURCE	SOURCE	IDENTIFIER
Bacterial and virus strains		
BL21(DE3) chemically competent <i>E.coli</i>	Agilent	Cat# 200131
Mach1 Chemically Competent <i>E.coli</i>	ThermoFisher	Cat# C862003?
Subcloning Efficiency DH5alpha Chemically Competent <i>E.coli</i>	ThermoFisher	Cat# 18265017
Chemicals, peptides, and recombinant proteins		
6xHis-NcKar9N	this study	N/A
6xHis-NcKar9N-F288A-F344A	this study	N/A
6xHis-NcKar9N-S190E-T195E-S225E	this study	N/A
Deposited data		
Crystal structure of <i>N.castellii</i> Kar9 N-terminal domain	https://www.rcsb.org	7AG9
Experimental models: Organisms/strains		
<i>S. cerevisiae</i> strain CFP-Tub1:Trp1 kar9::His3	Manatschal et al., 2016 and this study	yYB8597, yYB13801, yYB13802
<i>S. cerevisiae</i> strain CFP-Tub1:Trp1 kar9::Kar9-wt-mNeonGreen:NatNT2	this study	yYB16072, yYB16692, yYB16693
<i>S. cerevisiae</i> strain CFP-Tub1:Trp1 kar9::NcKar9-wt-mNeonGreen:NatNT2	this study	yYB16773, yYB16774, yYB16773-c3
<i>S. cerevisiae</i> strain CFP-Tub1:Trp1 kar9::NcKar9-F288A-F344A-mNeonGreen:NatNT2	this study	yYB16775, yYB16776, yYB16775-c4
<i>S. cerevisiae</i> strain CFP-Tub1:Trp1 kar9::NcKar9-S190E T195E S225E-mNeonGreen:NatNT2	this study	yYB16777, yYB16777-nc1, yYB16777-nc3
<i>S. cerevisiae</i> strain CFP-Tub1:Trp1 dyn1::HphNT1	this study	yYB11690, yYB16548
<i>S. cerevisiae</i> strain CFP-Tub1:Trp1 kar9::Kar9-F195A F292A L334A-mNeonGreen:NatNT2	this study	yYB16740, yYB16741, yYB16740-c3
<i>S. cerevisiae</i> strain CFP-Tub1:Trp1 kar9::Kar9-S197E-mNeonGreen:NatNT2	this study	yYB16778, yYB16779, yYB16778-c3

<i>S. cerevisiae</i> strain CFP-Tub1:Trp1 kar9::Kar9-S197E T202E S229E-mNeonGreen:NatNT2	this study	yYB16177, yYB16694, yYB16695
<i>S. cerevisiae</i> strain CFP-Tub1:Trp1 kar9::NcKar9-wt:Ura3	this study	yYB16780, yYB16781, yYB16780-c3
<i>S. cerevisiae</i> strain CFP-Tub1:Trp1	this study	yYB8594, yYB8595, yYB8596
<i>S. cerevisiae</i> strain CFP-Tub1:Trp1 kar9::NcKar9-F288A-F344A:Ura3	this study	yYB16784, yYB16785, yYB16784-c3
<i>S. cerevisiae</i> strain CFP-Tub1:Trp1 kar9::NcKar9-S190E T195E S225E:Ura3	this study	yYB16786, yYB16787, yYB16786-nc8
<i>S. cerevisiae</i> strain CFP-Tub1:Trp1 kar9::Kar9-wt-3xmKate:HphNT2 Myo2-998-GFP	this study	yYB15060
<i>S. cerevisiae</i> strain CFP-Tub1:Trp1 kar9::Kar9-S197E T202E S229E-3xmKate:HphNT2 Myo2-998-GFP	this study	yYB17128, yYB17128-c2
<i>S. cerevisiae</i> strain CFP-Tub1:Trp1 kar9::ATF1cc-Kar9tail(405)-3xmKate:HphNT2 Myo2-998-GFP	this study	yYB17129, yYB17129-c2
<i>S. cerevisiae</i> strain CFP-Tub1:Trp1 kar9::Kar9tail(405)-mNeonGreen:NatNT	this study	yYB17130, yYB17130-c3, yYB17130-c5
<i>S. cerevisiae</i> strain CFP-Tub1:Trp1 kar9::Kar9tail(405)-3xmKate:HphNT2 Myo2-998-GFP	this study	yYB17131, yYB17131-c4
Recombinant DNA		
pSPCm-2-6xHis-NcKar9N	this study	SE23_042
pSPCm-2-6xHis-NcKar9N-F288A-F344A	this study	SE23_043
pSPCm-2-6xHis-NcKar9N-S190E-T195E-S225E	this study	pYB2448/SE23_029
pOM40	(Gauss R, 2004)	-
Software and algorithms		
ImageJ/Fiji	(Schindelin et al., 2012)	https://fiji.sc/
softWoRX 6.5.2	Cytiva	N/A
Prism 9	GraphPad	https://www.graphpad.com/

Excel 16	Microsoft	https://www.office.com/
Unicorn 5	Cytiva	https://www.cytivalifesciences.com/en/us/shop/unicorn-5-31-p-01433
XDS	(Kabsch, 2010)	https://xds.mr.mpg.de/
PHENIX	(Adams et al., 2010)	http://www.phenix-online.org/
COOT	(Emsley and Cowtan, 2004)	https://www2.mrc-lmb.cam.ac.uk/personal/pemsley/coot/
CCP4	(Collaborative Computational Project, 1994)	https://www.ccp4.ac.uk/
TLS Motion Determination server	(Painter and Merritt, 2006)	http://skuld.bmsc.washington.edu/~tlsmd/
PyMOL	Schrödinger	https://www.schrodinger.com/products/pymol
PISA	(Krissinel and Henrick, 2007)	https://www.ebi.ac.uk/pdbe/pisa/
ASTRA 6	Wyatt Technology	https://www.wyatt.com/products/software/astra.html
Global3	Applied Photophysics	https://www.photophysics.com/support-and-service/documents-and-software/global-3-thermal-global-analysis-software